AIP | Physics of Plasmas

Nuclear imaging of the fuel assembly in ignition experiments

G. P. Grim, N. Guler, F. E. Merrill, G. L. Morgan, C. R. Danly et al.

Citation: Phys. Plasmas **20**, 056320 (2013); doi: 10.1063/1.4807291
View online: http://dx.doi.org/10.1063/1.4807291
View Table of Contents: http://pop.aip.org/resource/1/PHPAEN/v20/i5
Published by the American Institute of Physics.

Nuclear imaging of the fuel assembly in ignition experiments[a)]

G. P. Grim,[1,b)] N. Guler,[1] F. E. Merrill,[1] G. L. Morgan,[1] C. R. Danly,[1] P. L. Volegov,[1] C. H. Wilde,[1] D. C. Wilson,[1] D. S. Clark,[2] D. E. Hinkel,[2] O. S. Jones,[2] K. S. Raman,[2] N. Izumi,[2] D. N. Fittinghoff,[2] O. B. Drury,[2] E. T. Alger,[2] P. A. Arnold,[2] R. C. Ashabranner,[3] L. J. Atherton,[2] M. A. Barrios,[2] S. Batha,[1] P. M. Bell,[2] L. R. Benedetti,[2] R. L. Berger,[2] L. A. Bernstein,[2] L. V. Berzins,[2] R. Betti,[4] S. D. Bhandarkar,[2] R. M. Bionta,[2] D. L. Bleuel,[2] T. R. Boehly,[4] E. J. Bond,[2] M. W. Bowers,[2] D. K. Bradley,[2] G. K. Brunton,[2] R. A. Buckles,[5] S. C. Burkhart,[2] R. F. Burr,[2] J. A. Caggiano,[2] D. A. Callahan,[2] D. T. Casey,[2] C. Castro,[2] P. M. Celliers,[2] C. J. Cerjan,[2] G. A. Chandler,[6] C. Choate,[2] S. J. Cohen,[2] G. W. Collins,[2] G. W. Cooper,[7] J. R. Cox,[2] J. R. Cradick,[5] P. S. Datte,[2] E. L. Dewald,[2] P. Di Nicola,[2] J. M. Di Nicola,[2] L. Divol,[2] S. N. Dixit,[2] R. Dylla-Spears,[2] E. G. Dzenitis,[2] M. J. Eckart,[2] D. C. Eder,[2] D. H. Edgell,[4] M. J. Edwards,[2] J. H. Eggert,[2] R. B. Ehrlich,[2] G. V. Erbert,[2] J. Fair,[2] D. R. Farley,[2] B. Felker,[2] R. J. Fortner,[2] J. A. Frenje,[8] G. Frieders,[2] S. Friedrich,[2] M. Gatu-Johnson,[8] C. R. Gibson,[9] E. Giraldez,[9] V. Y. Glebov,[4] S. M. Glenn,[2] S. H. Glenzer,[2] G. Gururangan,[2] S. W. Haan,[2] K. D. Hahn,[6] B. A. Hammel,[2] A. V. Hamza,[2] E. P. Hartouni,[2] R. Hatarik,[2] S. P. Hatchett,[2] C. Haynam,[2] M. R. Hermann,[2] H. W. Herrmann,[1] D. G. Hicks,[2] J. P. Holder,[2] D. M. Holunga,[2] J. B. Horner,[2] W. W. Hsing,[2] H. Huang,[9] M. C. Jackson,[2] K. S. Jancaitis,[2] D. H. Kalantar,[2] R. L. Kauffman,[2] M. I. Kauffman,[10] S. F. Khan,[2] J. D. Kilkenny,[9] J. R. Kimbrough,[2] R. Kirkwood,[2] J. L. Kline,[1] J. P. Knauer,[4] K. M. Knittel,[2] J. A. Koch,[2] T. R. Kohut,[2] B. J. Kozioziemski,[2] K. Krauter,[2] G. W. Krauter,[2] A. L. Kritcher,[2] J. Kroll,[2] G. A. Kyrala,[1] K. N. La Fortune,[2] G. LaCaille,[2] L. J. Lagin,[2] T. A. Land,[2] O. L. Landen,[2] D. W. Larson,[2] D. A. Latray,[2] R. J. Leeper,[6] T. L. Lewis,[2] S. LePape,[2] J. D. Lindl,[2] R. R. Lowe-Webb,[2] T. Ma,[2] B. J. MacGowan,[2] A. J. MacKinnon,[2] A. G. MacPhee,[2] R. M. Malone,[10] T. N. Malsbury,[2] E. Mapoles,[2] C. D. Marshall,[2] D. G. Mathisen,[2] P. McKenty,[4] J. M. McNaney,[2] N. B. Meezan,[2] P. Michel,[2] J. L. Milovich,[2] J. D. Moody,[2] A. S. Moore,[11] M. J. Moran,[2] K. Moreno,[9] E. I. Moses,[2] D. H. Munro,[2] B. R. Nathan,[2] A. J. Nelson,[7] A. Nikroo,[9] R. E. Olson,[6] C. Orth,[2] A. E. Pak,[2] E. S. Palma,[2] T. G. Parham,[2] P. K. Patel,[2] R. W. Patterson,[2] R. D. Petrasso,[8] R. Prasad,[2] J. E. Ralph,[2] S. P. Regan,[4] H. Rinderknecht,[8] H. F. Robey,[2] G. F. Ross,[2] C. L. Ruiz,[6] F. H. Séguin,[8] J. D. Salmonson,[2] T. C. Sangster,[4] J. D. Sater,[2] R. L. Saunders,[2] M. B. Schneider,[2] D. H. Schneider,[2] M. J. Shaw,[2] N. Simanovskaia,[2] B. K. Spears,[2] P. T. Springer,[2] C. Stoeckl,[4] W. Stoeffl,[2] L. J. Suter,[2] C. A. Thomas,[2] R. Tommasini,[2] R. P. Town,[2] A. J. Traille,[5] B. Van Wonterghem,[2] R. J. Wallace,[2] S. Weaver,[2] S. V. Weber,[2] P. J. Wegner,[2] P. K. Whitman,[2] K. Widmann,[2] C. C. Widmayer,[2] R. D. Wood,[2] B. K. Young,[2] R. A. Zacharias,[2] and A. Zylstra[8]

[1]*Los Alamos National Laboratory, Los Alamos, New Mexico 87545, USA*
[2]*Lawrence Livermore National Laboratory, Livermore, California 94551-0808, USA*
[3]*Sandia National Laboratory, Livermore, California 94551, USA*
[4]*Laboratory for Laser Energetics, University of Rochester, Rochester, New York 14623, USA*
[5]*National Security Technologies, LO, Livermore, California 94550, USA*
[6]*Sandia National Laboratory, Albuquerque, New Mexico 87123, USA*
[7]*Chemical and Nuclear Engineering Department, University of New Mexico, Albuquerque, New Mexico 87131, USA*
[8]*Plasma Science and Fusion Center, Massachusetts Institute of Technology, Cambridge, Massachusetts 2139, USA*
[9]*General Atomics, San Diego, California 92186, USA*
[10]*National Security Technologies, LAO, Los Alamos, New Mexico 87544, USA*
[11]*AWE, Aldermaston, Reading, Berkshire RG7 4PR, United Kingdom*

(Received 14 December 2012; accepted 23 April 2013; published online 31 May 2013)

First results from the analysis of neutron image data collected on implosions of cryogenically layered deuterium-tritium capsules during the 2011-2012 National Ignition Campaign are reported. The data span a variety of experimental designs aimed at increasing the stagnation pressure of the central hotspot and areal density of the surrounding fuel assembly. Images of neutrons produced by deuterium–tritium fusion reactions in the hotspot are presented, as well as images of neutrons that scatter in the surrounding dense fuel assembly. The image data are compared with 1D and 2D model predictions, and consistency checked using other diagnostic data. The results indicate that the size of the fusing hotspot is consistent with the model predictions, as well as other imaging data, while the

[a)]Paper BI3 3, Bull. Am. Phys. Soc. **57**, 25 (2012).
[b)]Invited speaker. Electronic mail: gpgrim@lanl.gov

overall size of the fuel assembly, inferred from the scattered neutron images, is systematically smaller than models' prediction. Preliminary studies indicate these differences are consistent with a significant fraction (20%–25%) of the initial deuterium-tritium fuel mass outside the compact fuel assembly, due either to low mode mass asymmetry or high mode 3D mix effects at the ablator-ice interface. [http://dx.doi.org/10.1063/1.4807291]

I. INTRODUCTION

The goal of indirectly driven inertial confinement fusion experiments at the National Ignition Facility (NIF) is to obtain thermonuclear ignition using a small mass, ~170 μg, of hydrogen isotopes.[1] The process begins with the 192 beam, 351 nm, NIF laser which illuminates a high-Z cavity (hohlraum) producing a flux of soft X-rays. These X-rays ablate the outer surface of a ~2 mm diameter plastic shell, or ablator, containing a cryogenically formed deuterium-tritium ice shell approximately 70 μm thick. As the outside of the ablator is accelerated outwards, the balance of the mass recoils inward, compressing the remnant deuterium-tritium vapor at the center of the capsule. The goal is to accelerate the assembly through a peak velocity of ~370 km/s,[2,3] before deceleration and stagnation, compressing the initial gas volume by a factor of 35. The **pdV** work performed on the vapor raises the central temperature of the assembly to ~3 keV, initiating T(D,n)α reactions. The goal is to initiate a propagating wave of fusion reactions in the dense deuterium-tritium shell via sustained heating through alpha-particle energy deposition. To optimize the experimental program, the National Ignition Campaign (NIC) was created with a defined set of goals, requirements, and experimental plans.[2–4] During 2011, initial results from the NIC experimental program were published by Glenzer *et al.*[5] and Mackinnon *et al.*[6]

Results from ignition experiments performed between December 2011 and September 2012, referred to below as the 2012 data set, are reported here. These results focus on nuclear performance with emphasis on the size and shape of the implosion using the neutron imaging diagnostic.[7–10] Rather than focus on detailed analysis of specific shots,[11] we treat the 2012 data as a set, reporting on trends within the data and perform statistical comparisons with model predictions. In Sec. II, we briefly describe the neutron imaging technique, including image formation and reconstruction. In Sec. III, we describe a simple 1D model of the fuel assembly, based on neutron imaging data, and define the geometric down scatter ratio (DSR). In Sec. IV, we report on image data collected during 2012 ignition experiments and compare these data with the 1D model, as well as 2D post-shot simulations. Section V summarizes the discrepancies that arise with these comparisons and summarizes the conclusions drawn from these comparisons. Finally, a summary of results and conclusions is presented in Sec. VI.

II. NEUTRON IMAGING

Details on the development and implementation of the NIF neutron imaging diagnostic have been documented in a number of publications.[7–10] Presented below is a brief overview of the imaging system and initial data processing.

A. Image formation

The primary task of the NIF neutron imaging diagnostic[12] is to produce 2D images of primary fusion neutrons, as well as neutrons that scatter within the dense assembly of cryogenically layered implosions at the NIF. Time-of-flight gating is used to discriminate between primary and scattered neutrons. For most of the data presented below, the imaging system was gated to observe neutrons with kinetic energies between 13 and 17 MeV (primary) and 6 to 12 MeV (scattered). The primary neutron image gate is wider than used for time-of-flight diagnostics (13–15 MeV), due to the gating speed of the imaging system. The small number of neutrons with kinetic energy greater than 15 MeV in these implosions does not result in a systematic bias of the image data relative to the time-of-flight data. The diagnostic was designed to operate at a minimum primary yield of 1×10^{15} neutrons, with a "point resolution" of 14 μm near the peak of signal intensity. To accomplish this goal, the system uses a compound aperture[13] of 20 pinholes and three penumbral apertures. For 14 MeV neutrons, the approximate source plane resolution of the pinholes is 19 μm. For neutrons between 7 and 15 MeV, the total scattering cross section in the Au aperture varies by 5% from the 14 MeV value, maintaining similar resolution over this range. For neutrons between 6 and 7 MeV, the total scattering cross section is rising with decreasing energy, deviating by 15% at 6 MeV, resulting in improved resolution. For the analyses included here, we assume the pinhole point-spread function is constant versus neutron energy. The array of pinhole centerlines was designed to converge to a point 26.5 cm in front of the aperture. To accommodate a 200 μm field of view at the source plane, and to provide tolerance to aperture misalignment, the front of the aperture is located 32.5 cm from the target.

Fig. 1 shows the neutron imaging system detector, housed outside the NIF building, in the "NI annex." Neutrons enter the annex from the upper left, through the final line-of-site collimator, passing through a pair of paddle shaped, neutron time-of-flight detectors, and then into the imaging detector. The resolved neutron flux is detected in a 5 cm long by 16×16 cm^2 organic scintillator, constructed from a coherent array of 250 μm diameter scintillating fibers. The recoil lengths of elastically scattered protons can extend several millimeters in the scintillator, so the imaging scintillator mid-plane is positioned 2802.5 cm from the target to provide a system magnification of 85.2 for the pinhole images. To capture two images, light from each face of the

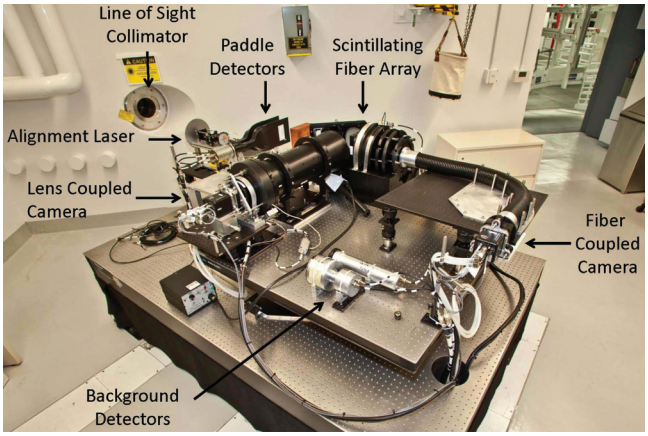

FIG. 1. The detector system for the NIF neutron imaging diagnostic. Neutrons exit the collimated line-of-site in the upper left, pass through paddle shaped time-of-flight detectors, and are imaged in the scintillating fiber array, indicated by the arrows.

fiber scintillator array is collected. Scintillation light, correlated with the neutron kinetic energy gates above, is sampled by gated micro-channel plate image intensifiers (MCPII) and subsequently digitized using CCD cameras.

B. Image processing

Prior to physics analysis, images must be corrected for both instrument and image formation response functions. Corrections include electronic pedestal subtraction, non-uniformity correction (flat-field), and spatial dewarping. We also replace localized, sub-resolution, hot-spots, a.k.a. "stars," with a neighborhood mean to remove defects caused by the scattered radiation environment near the CCD. Data for dewarping were collected by radiographing a regular grid of apertures through a thick copper block using 14 MeV neutrons from a deuterium-tritium filled exploding pusher type shot. These data are used to absolutely register the primary and scattered neutron images to an accuracy of $\pm 2.5\,\mu$m at the object plane. Exploding pusher shots (low areal density) are also used to directly measure the scintillator afterglow from 14 MeV neutrons during the time window corresponding to the arrival of 6–12 MeV neutrons from the source. After co-registration of the primary and scattered images, 1.4% of the primary image is subtracted from the scattered image to correct for afterglow.

Since the scintillator is 50 mm thick, a fraction of the neutrons will undergo multiple scatters. Multiple scattering produces a low-intensity, long range blur of the image field. Given the low spatial frequency of the blur, rather than deconvolve this response, we fit the inter-aperture light field, assuming the blur originates from neutrons passing through the penumbral apertures, and then subtract the fit from the image field.

After the instrument and image formation corrections are applied, the array of images is analyzed to determine the position of the source relative to each aperture centerline. The images formed by the set of pinholes most closely pointed at the source are inverted to source plane distributions using a Maximum Likelihood algorithm.[14–16] Since the aperture body is thick (20 cm), the point spread function depends on the location of the source relative to the axis of the pinhole, which is readily accommodated by the Maximum Likelihood approach. Detailed characterization and modeling studies indicate that near peak signal intensity, the system point resolution after inversion is 12 μm for primary yields greater than 3×10^{14} neutrons. Statistics and systematic effects, e.g., aperture manufacturing, pointing, etc., degrade the point resolution to $\sim$18 μm at the 17% contour of these same images.

C. The 17% contour

In the image analyses reported, we define the lateral extent of an image by the closed contour at 17% of peak signal intensity within the image. This contour is low enough in signal strength to accurately represent the lateral extent of the source image, but strong enough to be unaffected by random noise outside the source. This choice is further motivated by noting that for a spherical source of radius R_0 and constant emissivity, the 1D Abel transform, which gives the 1D image of the source as a function radius is: $2\sqrt{R_0^2 - r^2}$. The lateral extent of this function at 17% of the peak amplitude measures 98.5% of R_0, enclosing 95% of the volume of the source. Simulated images using transport Monte Carlo tools,[17–19] indicate that for a wide variety of density configurations and using a concentric shell geometry, the 17% contour of scattered neutron images represents approximately 90% of the lateral extent of the dense scattering volume. This systematic correction is used in the down scatter ratio predictions from the 1D model described section III.

1. Legendre polynomial fit

To simplify the mathematical representation of the contour, a finite Legendre polynomial expansion, Eq. (1), is used, where θ is the polar angle in the plane orthogonal to the neutron imaging line-of-site, $L_l(\theta)$ is the Legendre polynomial of order l, and P_l is its corresponding coefficient and fit parameter in the expansion

$$r_{17\%}(\theta) = \sum_{l=0}^{L} P_l \cdot L_l(\theta). \quad (1)$$

For the data below, the fit is performed out to mode 6, i.e., $L_6(\theta)$, with the constraint that $P_1 = 0$, which determines the location of the contour center. The process of the fit is illustrated in Fig. 2. Fig. 2(a) shows the 17% of peak contour identified on a sample image. One possible set of independent samples of the contour radius is shown in Fig. 2(b). The samples are independent if they are separated along the contour by the system resolution Δ. Each sample generates a radial measurement, r_i, at discrete angles θ_i, with radial uncertainty given by $\Delta/2\sqrt{2\ln 2}$. These samples are then fit using Eq. (1). Fig. 2(c) shows the results of a typical fit, with the first two even modes illustrated. The parameter P_0 is the mean radius of the contour, and P_2 is the deviation from this mean radius along the polar, or $\theta = 0$, direction.

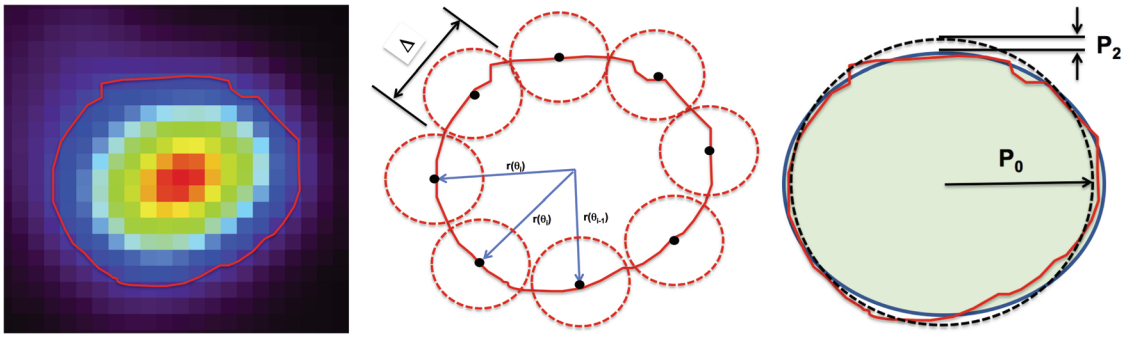

(a) 17% Contour (b) Contour sampling (c) Resulting fit

FIG. 2. Illustration of contour fitting with finite resolution. Fig. 2(a) shows the 17% contour; Fig. 2(b) shows the contour sampled with independent measures of the radial positions as a function of θ; and Fig. 2(c) shows the resultant fit using the first two even modes of the Legendre polynomial expansion.

2. Accuracy of Legendre coefficients

A conceptual exercise allows for a simple estimate of fit parameter accuracy based on system resolution. The number of independent samples, of size Δ, along a contour given by, $r(\theta) = P_0 + P_2 \cdot L_2(\theta)$, is approximated by

$$N_{samp} \approx \frac{2\pi\sqrt{\frac{(P_0+P_2)^2+(P_0-P_2/2)^2}{2}}}{\Delta}. \quad (2)$$

Letting Δ represent the full width at half maximum of a Gaussian distributed error on the radial measurement, the P_0 uncertainty may be estimated by

$$\delta P_0 = \frac{\Delta}{2\sqrt{2\ln 2(N_{samp}-1)}}. \quad (3)$$

Although studies have shown that the point resolution of the neutron imaging system is 12 μm near the peak of the image, these studies have also shown that at the 17% contour, statistical, and systematic effects degrade the point resolution to ~18 μm. Thus, a contour with a 27 μm P_0 will be independently sampled by 9 and 18 μm resolution elements, resulting in a P_0 estimated uncertainty of ≈2.6 μm. This estimate is in good agreement with replicate trials studies, where contours of constant intensity are generated at a variety of different P_0 and P_2 values. These contours are randomly sampled with different resolution sizes, Δ, and fit to the Legendre polynomial expansion using a least squares fitting algorithm. Fig. 3 shows the histogram fit P_0's from 2000 trials using the values from the above example, i.e., $P_0 = 27$ μm and $\Delta = 18$ μm. The gaussian fit to the ensemble yields $\delta P_0 = 2.9$ μm, in good agreement with the above estimate.

III. EMPIRICAL 1D FUEL ASSEMBLY MODEL

To explore the logical consistency of the image data with other nuclear data, we employ a simple 1D model, which is illustrated in Fig. 4(a). In this model, we identify two characteristic regions, the central hot (~2–4 keV) core (red), where fusion reactions occur, and the surrounding cold, dense deuterium-tritium shell (blue). To create this model from the 2D image data, we construct surfaces of revolution using the 17% contour. Since the NIF neutron imaging system views the imploded capsule along a direction orthogonal to the hohlraum axis, the image contours are revolved around the axis parallel to the hohlraum axis and through their, $P_1 = 0$, centers, forming bounding surfaces for the corresponding volumes. Using the primary neutron yield, ion temperature, and burn width from either the Gamma Reaction History diagnostic[20] or gated X-ray imaging diagnostic,[21,22] state variables, including, density, pressure, and adiabat may be calculated. This approach is complementary to the more sophisticated approach of Cerjan *et al.*[11] which does not include the primary and scattered neutron image data. In this work, we use the image data to directly calculate the fuel assembly geometry. Using the assumption of deuterium-tritium mass conservation, the volume densities are then inferred. Combining the geometry and density data, down scattering ratios are calculated and compared with neutron time-of-flight data.

A. Density

The density of the central hot-spot, where the primary neutron yield is produced, is given by

$$n_{DT} = \left(\frac{Y_n}{\langle\overline{\sigma v}\rangle \tau_{rh} V_{hs}}\right)^{1/2}, \quad (4)$$

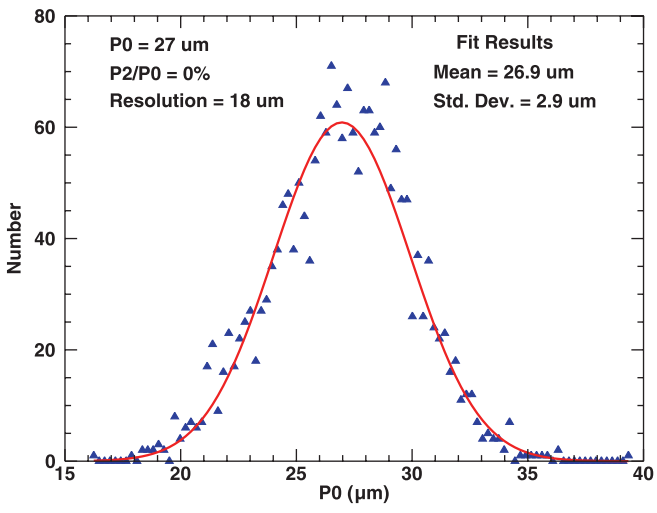

FIG. 3. Distribution of P_0 fit values from a replicate trials study.

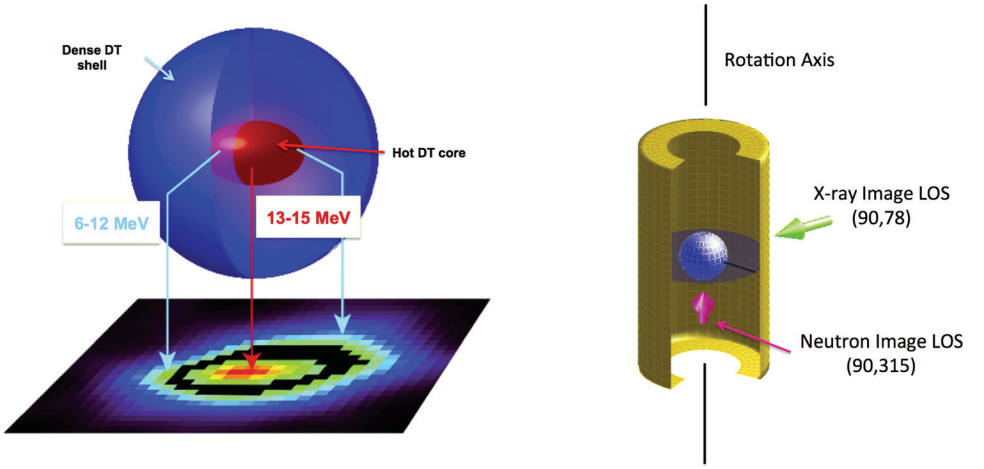

(a) Fuel assembly model (b) Imaging lines-of-site

FIG. 4. Fig. 4(a) illustrates the simple fuel assembly model used to describe the geometry of the neutron image source volumes. Fig. 4(b) illustrates the relationship between the X-ray and neutron imaging systems, which reside in the equatorial plane, orthogonal to the hohlraum axis. The angle of separation between the two imaging systems is 123°.

where Y_n is the measured total fusion yield, $\langle\overline{\sigma v}\rangle$ (Ref. 23) is the velocity averaged scattering cross section in units of cm^3/s, and V_{hs} is the hot-spot volume in units of cm^3. In this formula, n_{DT}^{hs} is the number density of deuterium-tritium ion pairs, assuming an equimolar distribution. For analyses below, the hot-spot volume, V_{hs}, is the volume contained within the surface of revolution defined by the 17% of peak intensity contour of the primary neutron image, as described in Sec. II C.

Assuming the balance of the initial deuterium-tritium mass resides in a shell just outside the hot-spot, the density of this shell is calculated using

$$\rho_{cf} = \frac{M_{DT}^{init} - \rho_{hs} V_{hs}}{V_{cf}}, \tag{5}$$

where M_{DT}^{init} is the initial deuterium-tritium mass in the capsule, ~170μg, ρ_{hs}, and V_{hs} are the hot-spot density, and volume, respectively, and V_{cf} is the cold fuel volume defined by the 17% contour of the scattered image data. For the cold fuel volume, 3D scattering simulations using MCNP have shown that the cold-fuel radius corresponds to 1.1 times the scattered image radius. With the volumes and densities now defined it is possible to form a simple model of the fuel assembly from which down scatter ratios may be calculated.

B. Geometric down scatter ratio

A simplifying approximation employed in the following is that the two volumes described above will be characterized by uniform density. This assumption is used due to the absence of spatial ion temperature measurements. Although this approximation does not provide for a detailed characterization of the microscopic properties of the fuel assembly, static MCNP, and dynamic 2D implosion simulations indicate that qualitative comparisons can be made with this model and that systematic trends can be quantified.

Fig. 5 summarizes the key concepts and components needed to calculate a geometric down scatter ratio, based on the neutron imaging data. The assembly has been simplified to two concentric spheres defined by the radii, $R_{hs} \equiv P_0^{hs}$, where fusion neutrons are born, and $R_{cf} \equiv 1.1 \cdot P_0^{cf}$, the dense deuterium-tritium shell where most neutrons scatter. The densities of these two volumes are n_{hs}, and n_{cf}, respectively. The lines illustrate how the fuel volume is sampled by the neutrons.

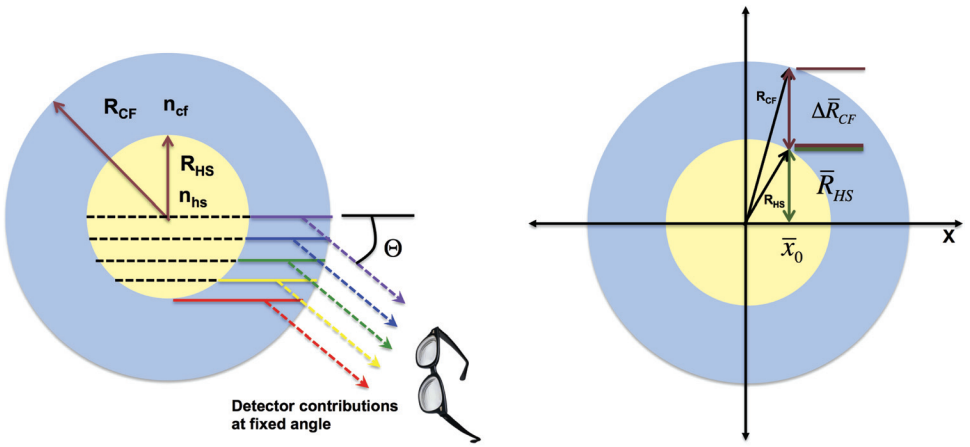

(a) Fuel regions and neutron paths. (b) Chordal paths

FIG. 5. Graphical illustration of the key components needed to calculate the geometric down scatter ratio using neutron imaging data. See text for full description.

For a detector located a large distance from the assembly, neutrons that undergo a single scatter through an angle, θ, into the detector acceptance were born as neutrons traveling to the right along the dashed and solid lines through the assembly. These neutrons may scatter at any point along either the dashed line through the hot-spot or along the solid line within the cold-fuel. The energy of the scattered neutron will be determined by the scattering process and the mass of the scattering center. At the NIF, the down scatter ratio determined by the neutron time-of-flight diagnostics is calculated using the measured flux of neutrons between 10 and 12 MeV, where elastic scattering off of deuterium and tritium ions is the dominant contribution.[24]

For a radial path through the equimolar deuterium-tritium fuel assembly, the ratio of the scattered neutron flux in the 10 to 12 MeV band to the un-collided flux is given by

$$\frac{\Phi_{coll}^{10-12}}{\Phi_{unc}} = \alpha^{10-12}\left(\exp\left\{\frac{N_A\bar{\sigma}_{DT}}{\bar{M}_{DT}}\left(\rho_{cf}\Delta R_{cf} + \rho_{hs}R_{hs}\right)\right\} - 1\right), \tag{6}$$

where N_A is Avogadro's number, $\bar{M}_{DT}$ is the average molar mass of a pair of deuterium and tritium ions, $\bar{\sigma}_{DT}$ (Ref. 25) is the average elastic scattering cross section of a 14 MeV neutron off of either a deuterium or tritium ion (=0.77 b), ρ_{cf} and ρ_{hs} are the gram densities of the cold-fuel and hot spot, respectively, R_{hs} is the hot spot radius, ΔR_{cf} is the thickness of the cold fuel along the radial, and finally, α^{10-12} is the fraction of scattered neutrons in the 10 to 12 MeV band

$$\alpha^{10-12} = \frac{\int_{10}^{12} dE\,\frac{d\sigma}{dE}}{\int dE\,\frac{d\sigma}{dE}}, \tag{7}$$

$$= 0.239. \tag{8}$$

Due to the relatively small fraction of scattered neutrons in the energy range between 13 to 15 MeV, the uncollided flux is approximated by this energy band, and the down-scattered ratio is defined as

$$DSR(10-12) = \frac{\Phi_{coll}^{10-12}}{\Phi^{13-15}} \approx \frac{\Phi_{coll}^{10-12}}{\Phi_{unc}}. \tag{9}$$

As can be seen in Fig. 5, a finite size hot-spot will generate non-radial contributions to the detected flux, which is not included in Eq. (6) above. To address this, Eq. (6) is generalized to the mean chordal path, through the fuel assembly, $\bar{R}_{hs} + \Delta\bar{R}_{cf}$, which occurs at the mean apothem x_0, in Fig. 5(b). The mean apothem is the density and path length weighted average of apothem across the hot-spot, i.e.,

$$\bar{x}_0 = \frac{\int_0^{R_{hs}} dx x\left(n_{hs}\sqrt{R_{hs}^2 - x^2} + n_{cf}\left(\sqrt{R_{cf}^2 - x^2} - \sqrt{R_{hs}^2 - x^2}\right)\right)}{\int_0^{R_{hs}} dx\left(n_{hs}\sqrt{R_{hs}^2 - x^2} + n_{cf}\left(\sqrt{R_{cf}^2 - x^2} - \sqrt{R_{hs}^2 - x^2}\right)\right)}, \tag{10}$$

which reduces to

$$\bar{x}_0 = \frac{4\left(R_{cf}^3 - \left(R_{cf}^2 - R_{hs}^2\right)^{3/2} - R_{hs}^3\left(1 - \frac{n_{hs}}{n_{cf}}\right)\right)}{6\left(R_{hs}\sqrt{R_{cf}^2 - R_{hs}^2} + R_{cf}^2\sin^{-1}\left(R_{hs}/R_{cf}\right)\right) - 3\pi R_{hs}^2\left(1 - \frac{n_{hs}}{n_{cf}}\right)}. \tag{11}$$

From this, the elements of the mean chordal path length are calculated using

$$\bar{R}_{hs} = \sqrt{R_{hs}^2 - \bar{x}_0^2}, \tag{12}$$

$$\Delta\bar{R}_{cf} = \sqrt{R_{cf}^2 - \bar{x}_0^2} - \sqrt{R_{hs}^2 - \bar{x}_0^2}, \tag{13}$$

and then substituted into Eq. (6) replacing R_{hs} and ΔR_{cf}, respectively.

Fig. 6 illustrates the agreement between the geometric down scatter ratio formula and a series of static fuel assemblies with varying radii, asymmetries, and densities, where were simulated using MCNP.[17] The horizontal axis of the figure is the down scatter ratio using energy resolved neutron tallies outside the fuel assembly, simulating a NIF neutron time-of-flight detector. The vertical axis is the geometric DSR, using only the simulated fuel geometry (P_0^{hs} and P_0^{cf}) and density (n^{hs} and n^{cf}). The number of histories generated was large enough that the tally error bars are smaller than the data marker. The red, $y = x$ line illustrates the agreement between the geometric formula and the tallied ratio over the range of down scatter values typically observed in ignition experiments at the NIF. The scatter is due to the non-spherical fuel assemblies simulated.

IV. IGNITION EXPERIMENT DATA

A. The primary neutron image

As described previously,[9,10] and in Sec. II A, images of primary neutrons are collected by gating one leg of the imaging system during the arrival time of neutrons with kinetic energies between 13 and 17 MeV. Fig. 7 shows a sample gallery of these images from the 2012 data set. The source plane pixel size of these images is 4 μm. The gallery shows the range of sizes and shapes collected to date.

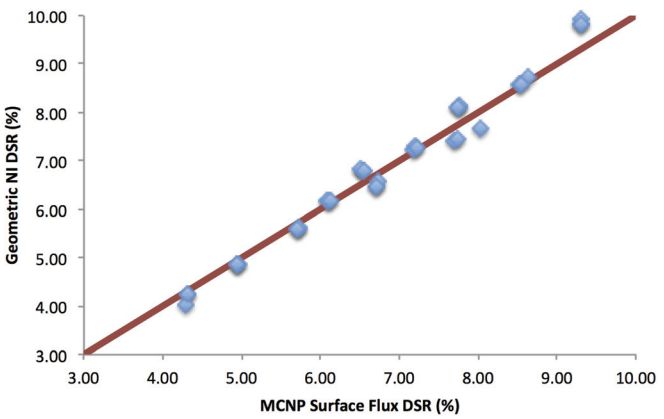

FIG. 6. Comparison of the geometric down scatter ratio formula with simulated neutron time-of-flight down scattered ratio data, using energy resolved neutron flux tallies in MCNP.

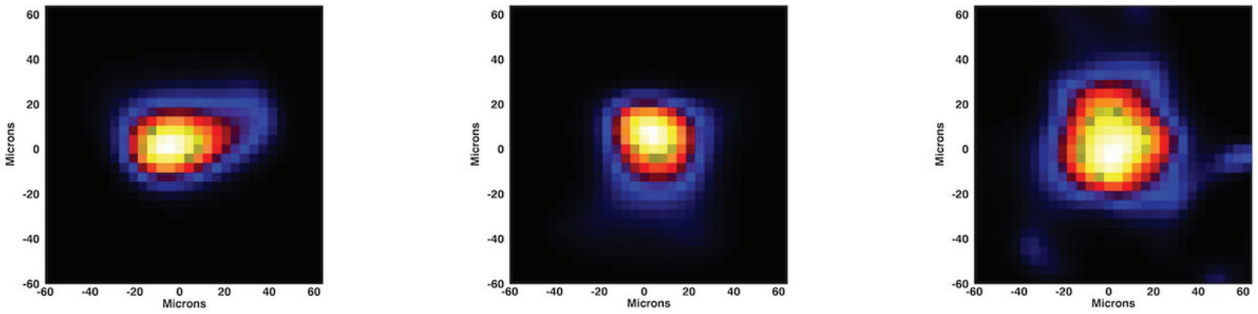

(a) Shot N111215: $P_0^{hs} = 28 \pm 3\ \mu m$, $P_2^{hs}/P_0^{hs} = -29 \pm 6\ \%$ (b) Shot N120321: $P_0^{hs} = 26 \pm 3\ \mu m$, $P_2^{hs}/P_0^{hs} = -10 \pm 6\ \%$ (c) Shot N120405: $P_0^{hs} = 27 \pm 3\ \mu m$, $P_2^{hs}/P_0^{hs} = 4 \pm 6\ \%$

FIG. 7. Gallery of primary (13–17 MeV) neutron images from layered cryogenic implosions between December 2011 and September 2012.

In the following, we have chosen to present the 2012 data as a set, with analyses based on trends and comparisons with models. We do this for several practical reasons. First, all data were collected at neutron yields below the design requirement of 1×10^{15}, varying from 9.8×10^{13} to 7.5×10^{14} neutrons. Further, because the diagnostic is relatively new, and calibration data relatively limited, a full understanding of the diagnostic's capabilities and limitations has yet to be realized, though considerable progress has been made. For example, the 17% contour fit, which includes the first six Legendre modes, i.e., P_0 through P_6, with the constraint, $P_1 = 0$, is only reported using the first two non-zero modes, P_0, and P_2, prohibiting higher mode shape analyses. To facilitate trend analysis across shots, we provide mean values for the size and shape of the various data sets, providing scale and a measure of variability of the data. It is important to note that the data are not identical experiments, and thus observed variations are not purely stochastic.

Fig. 8(a) shows the hot-spot (P_0^{hs}) data, along with the corresponding values from post-shot simulated neutron images. Data values are indicated by the blue circles, while simulation values are indicated by red squares. The values of P_0^{hs} vary from 23.8 μm to 33.5 μm, with a mean of 27.4 μm (blue dash), and a standard deviation of 2.4 μm. The error on an individual measurement varies between 3 and 4 μm, with contributions from background subtraction, statistics, resolution, aperture manufacturing, aperture pointing, and inversion algorithm systematics.[10,26] Fig. 8(b) shows the hot-spot shape data, expressed as the ratio, P_2^{hs}/P_0^{hs}. The values of P_2^{hs}/P_0^{hs} range between -0.37 and 0.21, with a mean value of -0.15 and a standard deviation of 0.21. The typical hot spot volume of a 2012 implosion is characterized by an oblate spheroid with a mean radius of 27.4 μm, and a radial deviation along the pole of -15%, or 4.4 μm.

Time integrated X-ray images,[27] filtered to energies ≥ 9 keV, were also collected. Hard X-ray images indicate where the fuel assembly is hot, and should produce data consistent with the neutron image size and shape. As illustrated in Fig. 4(b), equatorial X-ray images are collected along a different line of sight, rotated 123° around the hohlraum axis from the neutron image, and therefore projected asymmetries will be different between the two lines-of-sight, though P_0 values should be similar. The mean X-ray image size in the

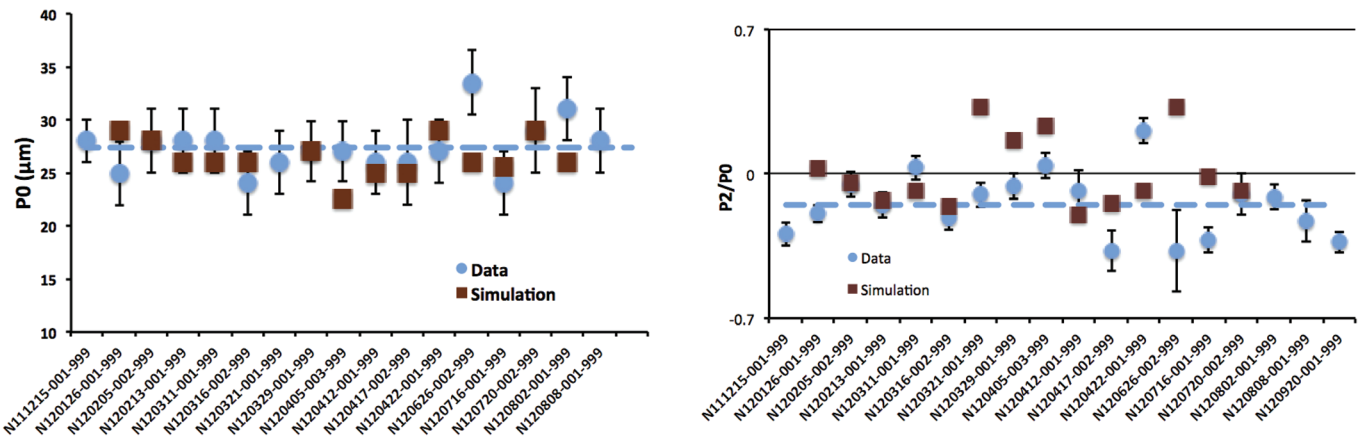

(a) Primary P_0^{hs} (b) Primary P_2^{hs}/P_0^{hs}

FIG. 8. Primary neutron image size and shape data from 2012. Fig. 8(a): P_0^{hs} from data (blue circles) and 2D simulated images (red squares), as well as the mean value for the data (blue dash). Fig. 8(b): P_2^{hs}/P_0^{hs} for data (blue circles) and 2D simulations (red squares) and the mean value for the data (blue dash).

above data, P_0^{X-ray}, is observed to be 27.3 μm, with 2.6 μm rms scatter, and the mean P_2^{X-ray}/P_0^{X-ray} is observed to be −0.09 with a rms of 0.08, both in good agreement with neutron image data. Since the neutron image data directly measure where fusion reactions are occurring, this result confirms the correctness of the assumption that the ≥9 KeV band of X-ray image data originates from the hot deuterium-tritium core rather than from outside the core.

Synthetic neutron images, for the 6–12 MeV, 10–12 MeV, and 13–17 MeV energy gates, were generated for comparison with data. The synthetic image results, indicated by the red squares in Fig. 8(a), were obtained by post-processing[28] 2D integrated hohlraum simulations,[29] where the radiation drive was tuned to match shock speed data from shock-timing experiments,[30] radius vs. time data from convergent ablator experiments,[31,32] and bang-time data from cryogenically layered deuterium-tritium implosions.[5,6,11] We have also generated synthetic images from high-resolution 2D capsule-only simulations[33] and the results are consistent with those presented. The simulated images were smoothed with a 10 μm FWHM Gaussian function to approximately match the diagnostic resolution of 12 μm, followed by the same analysis of the 17% contour as was done for the data. As can be seen in Fig. 8(a), the simulation results show good agreement with the data, having a mean radius (P_0^{hs}) of 26.4 μm, and standard deviation of 1.8 μm. On average the simulated images are symmetric with a $P_2^{hs}/P_0^{hs} = 0.01$, and a standard deviation of 0.18. A χ^2 analysis of the simulated and neutron image P_0^{hs} indicates that the simulated images perform well at predicting the actual data, with the probability that another set of data will measure a larger χ^2 than the current value is 93%.

The data shown in Fig. 8 were collected over a wide variety of experimental conditions aimed at increasing hot-spot pressure, which would correlate with a decreasing hot-spot size. The varying experimental conditions included changes to the laser drive by increasing the rise time of the 4th shock, lengthening the pulse, and increasing the peak power, as well as changes to the hohlraum materials and geometry. The data set shows no trend towards decreasing hot-spot size, or improved target performance, based on observed yields and ion temperature measurements.

B. The cold-fuel image

Images of neutrons scattered to energies lower than 12 MeV are collected in a second camera system viewing the scintillator. This second system is gated to view scintillation light coincident with neutrons arriving with kinetic energies between 6 and 12 MeV, except for shots N111215 and N120126, which used a 10–12 MeV gate. Fig. 9 shows a gallery of scattered neutron images from the 2012 data set. As expected, the scattered images are larger than the primary images, due to the dense deuterium-tritium volume surrounding the hot-spot. Absolute registration of the primary and scattered images shows that the 17% contours of the two images are concentric. The accuracy of the image co-registration is ±2.5 μm. Studies with neutron transport Monte-Carlo tools have shown that both the 10–12 MeV and 6–12 MeV energy images produce comparable contours of constant signal intensity, and the 17% contour contains, on average, 95% of the cold dense fuel.

Fig. 10 shows a summary of the P_0^{cf} and P_2^{cf}/P_0^{cf} measurements (blue circles), along with post-shot simulation estimates of these quantities (red squares). The set of data shown is reduced in number over the hot-spot image data due to the low yields in several of the shots. The mean P_0^{cf} value of these data is 37.8 μm, with a standard deviation of 3.9 μm. The error on an individual measurement varies between 3.5 μm and 5.5 μm, depending on yield. The sources of uncertainty in these data are similar to those for the primary image with the contribution from statistical uncertainties being larger. Fig. 10(b) shows the variation of the scattered image P_2^{cf}/P_0^{cf} data set. Similar to the primary image, the scattered image P_2^{cf}/P_0^{cf} varies from −0.31 to 0.2, but unlike the primary image, the mean value is −0.01 with a standard deviation of 0.11. For the analyses below, we treat the volume defined by the scattered image as a sphere. The apparent presence of higher mode components does not materially effect this approximation, since volume corrections of higher order modes contribute as their relative amplitudes cubed, i.e., $(P_i/P_0)^3$.

As mentioned, the red squares in Fig. 10(a) are the 2D simulated neutron image P_0^{cf} values. The values range from a minimum of 39 μm to a maximum of 50 μm, with a mean value of 44.5 μm and a rms scatter of 2.9 μm. On average,

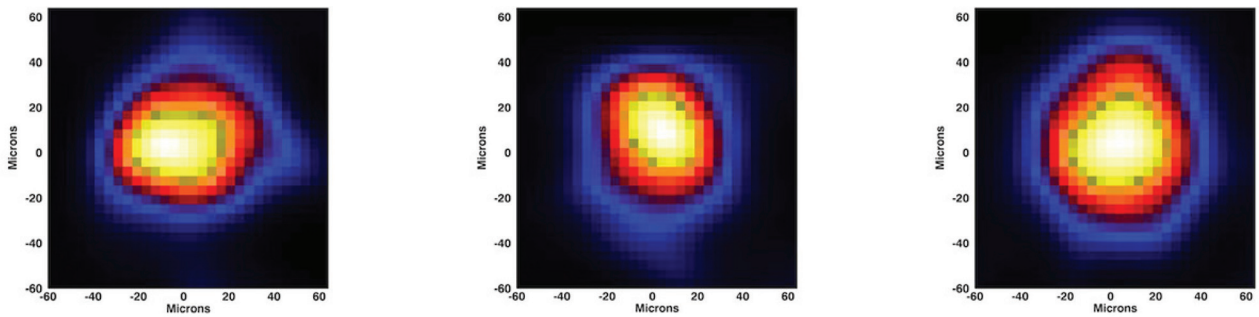

(a) Shot N111215: $P_0^{cf} = 43 \pm 6$ μm, $P_2^{cf}/P_0^{cf} = -1 \pm 6$ % (10–12 MeV)

(b) Shot N120321: $P_0^{cf} = 35 \pm 5$ μm, $P_2^{cf}/P_0^{cf} = 1 \pm 6$ %

(c) Shot N120405: $P_0^{cf} = 43 \pm 3$ μm, $P_2^{cf}/P_0^{cf} = 12 \pm 6$ %

FIG. 9. Gallery of scattered neutron images from layered cryogenic implosions between December 2011 and September 2012.

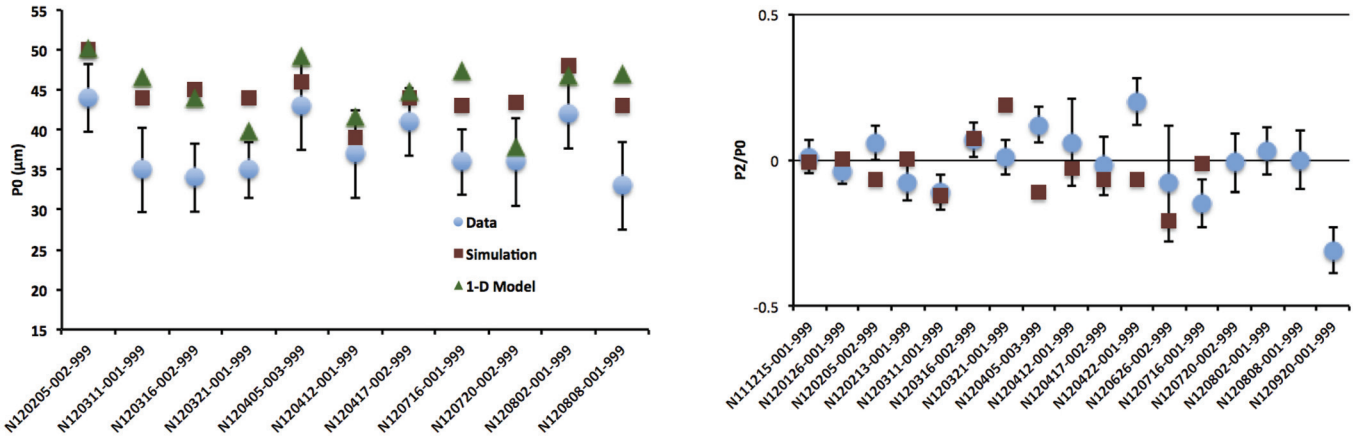

(a) Scattered Image P_0^{cf} (b) Scattered Image P_2^{cf}/P_0^{cf}

FIG. 10. Scattered neutron image size and shape data from the 2012 data set (blue circles), 2D post-shot simulations (red squares), and 1D model predictions (green triangles). Fig. 10(a) shows the scattered image P_0^{cf} data, while Fig. 10(b) shows scattered image P_2^{cf}/P_0^{cf} data.

the mean radius of the simulated images is $6.7 \pm 0.8\,\mu$m larger than the data. The discrepancy between the data and simulation is statistically significant. The χ^2 difference between the two sets is 28.7. Thus, the probability that an alternative set of data will produce a χ^2 as large as this is less than 3.7%, indicating that the models producing the simulated images do not describe the scattered image data. This discrepancy has implication with respect to the shell density, which will be discussed in Sec. IV C.

One possible explanation could be a systematic underestimate of the image size to due image statistics. Empirical characterization of the camera system, using image data from low yield implosions, indicate the lateral extent of a cold fuel assembly with uniform density should be sufficiently sampled to produce a significant image at primary yields of $\gtrsim 1.0$–1.5×10^{14} neutrons, though the error bars become large.

Using the simple 1D model described above, it is possible to calculate the expected scattered image P_0^{cf} needed to match the measured down scatter ratio of these experiments, indicated by the green triangles in Fig. 10(a). The measured down scattered ratio is determined using neutron time-of-flight diagnostics.[34] Not surprisingly, the geometric down scatter ratio predictions are systematically larger than the data and agree, reasonably, with the 2D simulation results, indicating that in these simulations a large fraction of the initial deuterium-tritium mass in the target is participating in the simulated scattered image. In studies by the authors of the 2D simulations used to generate the neutron images, it was found that the 17% contour of the corresponding simulated scattered image typically contained ~95% of the initial deuterium-tritium mass.

C. Dense shell geometry

In the simple 1D concentric shell model of the fuel assembly, the dense deuterium-tritium layer resides just outside the oblate spheroid defined by the hot-spot image and inside the sphere defined by the scattered fuel image. This volume may be characterized by a mean thickness, T_0, and the fractional deviation along the pole, $T_2/T_0 = (P_2^{cf} - P_2^{hs})/(P_0^{cf} - P_0^{hs})$. Fig. 11 shows the T_0 and T_2/T_0 data from the 2012 data set, where

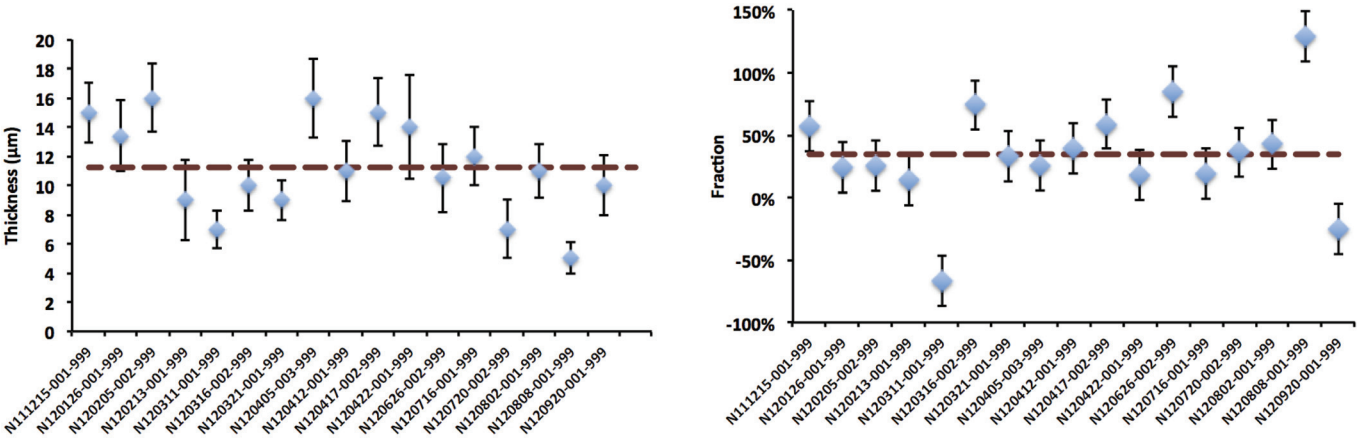

(a) Shell thickness: T_0 (b) Shell asymmetry: T_2/T_0

FIG. 11. Dense deuterium-tritium shell geometry created by taking the difference between the Legendre polynomial expansion of the scattered image and hot spot image at 17% contour.

the data with large P_0^{cf} error bars (low yield) is now included. The inferred shell thickness varies from 7 μm up to 18.7 μm. The mean thickness is 11.3 μm, with a rms scatter of 3.3 μm. Because of the oblate hot-spot, the shell thickness is prolate with $T_2/T_0 = 0.3$ and $\sigma_{rms} = 0.3$. A prolate shell results in differential attenuation of the radial 14 MeV neutron flux between the pole and the equator. The 2012 image data imply that the ratio of the polar to equatorial uncollided radial flux is given by $(1 - T_2/(2T_0))/(1 + T_2/T_0) = 0.7$. Experimental values would be closer to 1 due to the finite source size. In the analysis by Cerjan *et al.*,[11] detailed modeling of the fuel distribution for shot N120321, using nuclear activation[35] data, results in an asymmetric distribution of mass with high density regions accumulating at the poles and lower density regions on the equator. This configuration is consistent with the shell thickness data above.

D. Geometric downscattered ratio

As described in Sec. III B, the above geometry data may used to infer a geometric down scatter ratio based on the assumption that the deuterium-tritium fuel is uniformly distributed within the volumes calculated. The inferred geometric down scatter ratio data are shown in Fig. 12, indicated by the green diamonds. Also plotted are the NIF authorized down scatter ratio measurements, blue circles, as well as the 2D simulated down scattered ratios, red squares. Although the geometric down scatter data trend with the time-of-flight data, on average, they are 34% larger. The simulated neutron time-of-flight down scatter ratios show better agreement with data, but these also show a systematic excess of 27%. This last point is significant, as the 2D simulation data not only over predicts the neutron image size, but also over predicts the observed down scatter ratio, which is inconsistent with a simple 1D, mass conserving model of the fuel assembly.

V. DISCREPANT DATA SYNOPSIS

In the preceding sections, the image and down scattered ratio data were compared with predictions from a simple 1D model, and 2D state-of-the-art integrated hohlraum simulations. Significant discrepancies and inconsistencies exist between the data and model predictions with the most notable facts summarized below:

- The 2D simulated scattered image size is consistent with the inferred image size from the 1D model, using the hot-spot image size and neutron time-of-flight down scattered ratio data.
- The 2D simulated scattered image size is systematically larger than the data.
- The 2D simulated down scatter ratio is systematically larger than the data.
- The down scattered ratio inferred from the 1D model, using the hot-spot and scattered image sizes, is systematically larger than the 2D simulated down scatter ratio, (and therefore data).

By construction, the 1D model conserves initial deuterium-tritium mass within image volumes. The first item above indicates that the 2D simulations effectively conserve initial mass ($\geq 95\%$) within the image volumes as well. Since the 2D simulated down scatter ratios and simulated scattered image sizes both over predict data, resolving these discrepancies simultaneously, while conserving initial deuterium-tritium mass, is logically inconsistent. Thus, in the absence of unknown systematic effects, the scattered image data indicate that substantially less mass than the initial deuterium-tritium payload is present at stagnation.

Reducing the mass within the cold-fuel shell by 23.5% would eliminate the discrepancy between the data and the geometric down scatter ratio, though this represents a significant fraction of the fuel assembly, or close to 40 μg. Initial studies using 2D and 3D HYDRA simulations hint at several means of moving mass outside the 17% contour. For example, high-mode 2D mix at the ablator–fuel interface, seeded by surface roughness profiles 1–3 times larger than the measured outer surface metrology, could result in up to 25% of the fuel mass lying outside the 17% contour, lowering the geometric down scatter ratio closer to the observed values. A byproduct of interface mix is hot-spot shape (P_2^{hs}/P_0^{hs}) variability in the primary neutron image on the scale of 10%, which is also consistent with observed variations in the data. However, it was found that 2D mix did not change the P_0^{cf} of the 17% down scattered image contour from the unmixed case, even when the simulated surface roughness was increased multiple times over the measured value. Preliminary studies indicate that accounting for 3D mix could lower the size of the 17% down scattered image contour closer to the observed value, but more investigation is needed. An alternate explanation for the size discrepancy is that large low mode asymmetries, due to asymmetric drive conditions, could move as much as 20% of the payload mass up to the poles where it is kinematically more difficult for the D and T atoms to down scatter primary neutrons in a manner that contributes to an equatorial down scattered image. Preliminary studies indicate that when the fuel assembly is much thicker in the polar regions, the size of 17% contour of the 6–12 MeV image could be smaller than the lateral extent of the fuel assembly, but more investigation is needed.

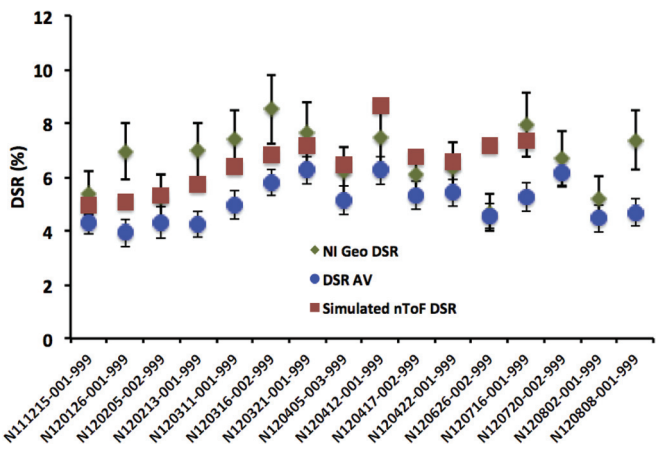

FIG. 12. Down scatter ratio data for layered cryogenic implosions. Blue circles are NIF neutron time-of-flight measurements, green diamonds are the inferred ratio using geometry data from the neutron imaging diagnostic, and the red squares are the results of 2D integrated hohlraum simulations.

VI. SUMMARY

The NIF neutron imaging system now routinely produces high quality neutron images of where 14 MeV neutrons are born and scattered in imploded deuterium-tritium fuel assemblies. Primary neutron images have been collected at yields as low as 9×10^{12}, and both primary and scattered neutron images have been collected on ignition experiments during the period from December 2011 and September 2012. The mean size and shape of the hot-spot, as characterized by Legendre mode decomposition, is: $P_0^{hs} = 27.4\,\mu$m, $(\sigma_{rms} = 2.4\,\mu$m), and P_2^{hs}/P_0^{hs} of -15%, $(\sigma_{rms} = 16\%)$, with no apparent size trend observed during the 2012 experiments. Ross pair filtered 9–11 KeV X-ray image data, as well as post-shot 2D simulations show excellent agreement with the primary neutron image data. The corresponding scattered image data are characterized by: $P_0^{cf} = 38.7\,\mu$m, $\sigma_{rms} = 3.3\,\mu$m, and P_2^{cf}/P_0^{cf} of -1%, $(\sigma_{rms} = 11\%)$. The scattered images produced by 2D simulations are significantly discrepant with the data, systematically over predicting the scattered image size by $6.7 \pm 0.8\,\mu$m. A simple 1D model was used to explore logical consistency of the image data with the down scatter data, as well as for analyzing the discrepancy between the 2D simulated images and data. Results of these analyses indicate that the mass participating in the scattered image formation is substantially less, by ~25%, than the initial payload. Preliminary simulation studies have shown that this reduced mass in the image formation process may originate with either low mode mass asymmetries within the fuel assembly, or possibly high mode mix at the ablator fuel interface. Further studies on these effects are ongoing.

ACKNOWLEDGMENTS

We would like to acknowledge the staff of the National Ignition Facility for their tireless effort to provide the highest-quality experimental data in a demanding and exacting environment under great time pressure. We would like to express our deepest thanks to the entire staff of the Target Diagnostics and Target Area Operations teams. In particular, we are deeply indebted to Dan Kalantar and Reg Wood for their relentless pursuit of perfect alignment of the neutron imaging diagnostic.

This work was performed for the U.S. Department of Energy, National Nuclear Security Administration and by the National Ignition Campaign partners; Lawrence Livermore National Laboratory (LLNL), University of Rochester-Laboratory for Laser Energetics (LLE), General Atomics (GA), Los Alamos National Laboratory (LANL), Sandia National Laboratory (SNL). Other contributors include Lawrence Berkeley National Laboratory (LBNL), Massachusetts Institute of Technology (MIT), Atomic Weapons Establishment (AWE), England, and Commissariat lnergie Atomique (CEA), France. Prepared by LANL under Contract No. DE-AC-52-06-NA25396, TSPA, LA-UR-13-21677, Prepared by LLNL under Contract No. DE-AC52-07NA27344.

[1]J. D. Lindl, *Inertial Confinement Fusion: The Quest for Ignition and Energy Gain Using Indirect Drive* (Springer, AIP, New York, NY, 1998).
[2]S. W. Haan, J. D. Lindl, D. A. Callahan, D. S. Clark, J. D. Salmonson, B. A. Hammel, L. J. Atherton, R. C. Cook, M. J. Edwards, S. Glenzer, A. V. Hamza, S. P. Hatchett, M. C. Herrmann, D. E. Hinkel, D. D. Ho, H. Huang, O. S. Jones, J. Kline, G. Kyrala, O. L. Landen, B. J. MacGowan, M. M. Marinak, D. D. Meyerhofer, J. L. Milovich, K. A. Moreno, E. I. Moses, D. H. Munro, A. Nikroo, R. E. Olson, K. Peterson, S. M. Pollaine, J. E. Ralph, H. F. Robey, B. K. Spears, P. T. Springer, L. J. Suter, C. A. Thomas, R. P. Town, R. Vesey, S. V. Weber, H. L. Wilkens, and D. C. Wilson, "Point design targets, specifications, and requirements for the 2010 ignition campaign on the national ignition facility," Phys. Plasmas **18**, 051001 (2011).
[3]M. J. Edwards, J. D. Lindl, B. K. Spears, S. V. Weber, L. J. Atherton, D. L. Bleuel, D. K. Bradley, D. A. Callahan, C. J. Cerjan, D. Clark, G. W. Collins, J. E. Fair, R. J. Fortner, S. H. Glenzer, S. W. Haan, B. A. Hammel, A. V. Hamza, S. P. Hatchett, N. Izumi, B. Jacoby, O. S. Jones, J. A. Koch, B. J. Kozioziemski, O. L. Landen, R. Lerche, B. J. MacGowan, A. J. MacKinnon, E. R. Mapoles, M. M. Marinak, M. Moran, E. I. Moses, D. H. Munro, D. H. Schneider, S. M. Sepke, D. A. Shaughnessy, P. T. Springer, R. Tommasini, L. Bernstein, W. Stoeffl, R. Betti, T. R. Boehly, T. C. Sangster, V. Y. Glebov, P. W. McKenty, S. P. Regan, D. H. Edgell, J. P. Knauer, C. Stoeckl, D. R. Harding, S. Batha, G. Grim, H. W. Herrmann, G. Kyrala, M. Wilke, D. C. Wilson, J. Frenje, R. Petrasso, K. Moreno, H. Huang, K. C. Chen, E. Giraldez, J. D. Kilkenny, M. Mauldin, N. Hein, M. Hoppe, A. Nikroo, and R. J. Leeper, "The experimental plan for cryogenic layered target implosions on the national ignition facility—the inertial confinement approach to fusion," Phys. Plasmas **18**, 051003 (2011).
[4]O. L. Landen, J. Edwards, S. W. Haan, H. F. Robey, J. Milovich, B. K. Spears, S. V. Weber, D. S. Clark, J. D. Lindl, B. J. MacGowan, E. I. Moses, J. Atherton, P. A. Amendt, T. R. Boehly, D. K. Bradley, D. G. Braun, D. A. Callahan, P. M. Celliers, G. W. Collins, E. L. Dewald, L. Divol, J. A. Frenje, S. H. Glenzer, A. Hamza, B. A. Hammel, D. G. Hicks, N. Hoffman, N. Izumi, O. S. Jones, J. D. Kilkenny, R. K. Kirkwood, J. L. Kline, G. A. Kyrala, M. M. Marinak, N. Meezan, D. D. Meyerhofer, P. Michel, D. H. Munro, R. E. Olson, A. Nikroo, S. P. Regan, L. J. Suter, C. A. Thomas, and D. C. Wilson, "Capsule implosion optimization during the indirect-drive national ignition campaign," Phys. Plasmas **18**, 051002 (2011).
[5]S. H. Glenzer, D. A. Callahan, A. J. Mackinnon, J. L. Kline, G. Grim, E. T. Alger, R. L. Berger, L. A. Bernstein *et al.*, "Cryogenic thermonuclear fuel implosions on the national ignition facility," Phys. Plasmas **19**, 056318-1 (2012).
[6]A. J. Mackinnon, J. L. Kline, S. N. Dixit, S. H. Glenzer, M. J. Edwards, D. A. Callahan, N. B. Meezan, S. W. Haan, J. D. Kilkenny, and T. Doeppner, "Assembly of high-areal-density deuterium-tritium fuel from indirectly driven cryogenci implosions," Phys. Rev. Lett. **108**, 215005-1 (2012).
[7]D. C. Wilson, C. R. Christensen, G. L. Morgan, M. D. Wilke, P. A. Bradley, and P. L. Gobby, "Goals for and design of a neutron pinhole imaging system for ignition capsules," Rev. Sci. Instrum. **74**, 1705–1708 (2003).
[8]G. Grim, C. Barnes, P. Bradley, C. Christensen, A. Hauer, G. Morgan, J. Oertel, M. Wilke, D. Wilson, C. Barrera, S. Haan, B. Hammel, J. Koch, R. Lerche, M. Moran, V. Glebov, T. Sangster, J.-L. Bourgade, L. Disdier, I. Lantuejoul, and O. Landoas, "Neutron imaging at the NIF," J. Phys. IV France **133**, 913–918 (2006).
[9]M. D. Wilke, S. H. Batha, P. A. Bradley, R. D. Day, D. D. Clark, V. E. Fatherley, J. P. Finch, R. A. Gallegos, F. P. Garcia, G. P. Grim, S. A. Jaramillo, A. J. Montoya, M. J. Moran, G. L. Morgan, J. A. Oertel, T. A. Ortiz, J. R. Payton, P. Pazuchanics, D. W. Schmidt, A. C. Valdez, C. H. Wilde, and D. C. Wilson, "The national ignition facility neutron imaging system," Rev. Sci. Instrum. **79**, 10E529 (2008).
[10]F. E. Merrill, D. Bower, R. Buckles, D. D. Clark, C. R. Danly, O. B. Drury, J. M. Dzenitis, V. E. Fatherley, D. N. Fittinghoff, R. Gallegos, G. P. Grim, N. Guler, E. N. Loomis, S. Lutz, R. M. Malone, D. D. Martinson, D. Mares, D. J. Morley, G. L. Morgan, J. A. Oertel, I. L. Tregillis, P. L. Volegov, P. B. Weiss, C. H. Wilde, and D. C. Wilson, "The neutron imaging diagnostic at NIF (invited)," Rev. Sci. Instrum. **83**, 10D317-1–6 (2012).
[11]C. Cerjan, P. T. Springer, and S. M. Sepke, "Integrated diagnostic analysis of inertial confinement fusion capsule performance," Phys. Plasmas **20**, 056319 (2013).
[12]C. Cerjan, S. Haan, S. Hatchett, and J. Koch, "Failure modes and diagnostic signatures working group - ignition diagnostics requirements update," Technical Report No. UCRL-TR-229780 (Lawrence Livermore National Laboratory, 2007).
[13]R. F. Wagner, D. G. Brown, and C. E. Metz, "On the multiplex advantage of coded source/aperture photon imaging," Proc. SPIE **314**, 72–76 (1981).
[14]A. P. Dempster, N. M. Laird, and D. B. Rubin, "Maximum likelihood from incomplete data via the EM algorithm," J. R. Stat. Soc., Ser. B **38**, 1–38 (1977).
[15]L. A. Shepp and Y. Vardi, "Maximum likelihood reconstruction for emission tomography," IEEE Trans. Med. Imaging **1**, 113–122 (1982).

[16]V. I. Gelfgat, E. Kosarev, and E. Podolyak, "Programs for signal recovery from noisy data using the maximum likelihood principle: I. General description," Comput. Phys. Commun. **74**, 335 (1993).
[17]J. Briesmeister *et al.*, *MCNP–A general Monte Carlo Code for Neutron and Photon Transport* (Los Alamos National Laboratory, 1986).
[18]D. B. Pelowitz *et al.*, "MCNPX user's manual, version 2.5.0," Technical Report No. LA-CP-05-0369 (Los Alamos National Laboratory, 2005).
[19]D. C. Wilson, G. P. Grim, I. L. Tregillis, M. D. Wilke, M. V. Patel, S. M. Sepke, G. L. Morgan, R. Hatarik, E. N. Loomis, C. H. Wilde, J. A. Oertel, V. E. Fatherley, D. D. Clark, D. N. Fittinghoff, D. E. Bower, M. J. Schmitt, M. M. Marinak, D. H. Munro, F. E. Merrill, M. J. Moran, T.-S. F. Wang, C. R. Danly, R. A. Hilko, S. H. Batha, M. Frank, and R. Buckles, "Modeling the national ignition facility neutron imaging system," Rev. Sci. Instrum. **81**, 10D335 (2010).
[20]H. W. Herrmann, N. Hoffman, D. C. Wilson, W. Stoeffl, L. Dauffy, Y. H. Kim, A. McEvoy, C. S. Young, J. M. Mack, C. J. Horsfield, M. Rubery, E. K. Miller, and Z. A. Ali, "Diagnosing inertial confinement fusion gamma ray physics (invited)," Rev. Sci. Instrum. **81**, 10D333 (2010).
[21]J. A. Oertel, R. Aragonez, T. Archuleta, C. Barnes, L. Casper, V. Fatherley, T. Heinrichs, R. King, D. Landers, F. Lopez, P. Sanchez, G. Sandoval, L. Schrank, P. Walsh, P. Bell, M. Brown, R. Costa, J. Holder, S. Montelongo, and N. Pederson, "Gated x-ray detector for the national ignition facility," Rev. Sci. Instrum. **77**, 10E308 (2006).
[22]S. Glenn, J. Koch, D. K. Bradley, N. Izumi, P. Bell, J. Holder, G. Stone, R. Prasad, A. MacKinnon, P. Springer, O. L. Landen, and G. Kyrala, "A hardened gated x-ray imaging diagnostic for inertial confinement fusion experiments at the national ignition facility," Rev. Sci. Instrum. **81**, 10E539 (2010).
[23]H.-S. Bosch and G. Hale, "Improved formulas for fusion cross-sections and thermal reactivities," Nucl. Fusion **32**, 611 (1992).
[24]M. G. Johnson, J. A. Frenje, D. T. Casey, C. K. Li, F. H. Séguin, R. Petrasso, R. Ashabranner, R. M. Bionta, D. L. Bleuel, E. J. Bond, J. A. Caggiano, A. Carpenter, C. J. Cerjan, T. J. Clancy, T. Doeppner, M. J. Eckart, M. J. Edwards, S. Friedrich, S. H. Glenzer, S. W. Haan, E. P. Hartouni, R. Hatarik, S. P. Hatchett, O. S. Jones, G. Kyrala, S. L. Pape, R. A. Lerche, O. L. Landen, T. Ma, A. J. MacKinnon, M. A. McKernan, M. J. Moran, E. Moses, D. H. Munro, J. McNaney, H. S. Park, J. Ralph, B. Remington, J. R. Rygg, S. M. Sepke, V. Smalyuk, B. Spears, P. T. Springer, C. B. Yeamans, M. Farrell, D. Jasion, J. D. Kilkenny, A. Nikroo, R. Paguio, J. P. Knauer, V. Y. Glebov, T. C. Sangster, R. Betti, C. Stoeckl, J. Magoon, M. J. Shoup III, G. P. Grim, J. Kline, G. L. Morgan, T. J. Murphy, R. J. Leeper, C. L. Ruiz, G. W. Cooper, and A. J. Nelson, "Neutron spectrometry—An essential tool for diagnosing implosions at the national ignition facility (invited)," Rev. Sci. Instrum. **83**, 10D308 (2012).
[25]M. Chadwick, M. Herman, P. Obložinský, M. Dunn, Y. Danon, A. Kahler, D. Smith, B. Pritychenko, G. Arbanas, R. Arcilla, R. Brewer, D. Brown, R. Capote, A. Carlson, Y. Cho, H. Derrien, K. Guber, G. Hale, S. Hoblit, S. Holloway, T. Johnson, T. Kawano, B. Kiedrowski, H. Kim, S. Kunieda, N. Larson, L. Leal, J. Lestone, R. Little, E. McCutchan, R. MacFarlane, M. MacInnes, C. Mattoon, R. McKnight, S. Mughabghab, G. Nobre, G. Palmiotti, A. Palumbo, M. Pigni, V. Pronyaev, R. Sayer, A. Sonzogni, N. Summers, P. Talou, I. Thompson, A. Trkov, R. Vogt, S. van der Marck, A. Wallner, M. White, D. Wiarda, and P. Young, "Endf/b-vii.1 nuclear data for science and technology: Cross sections, covariances, fission product yields and decay data," Nucl. Data Sheets **112**, 2887–2996 (2011), Special Issue on ENDF/B-VII.1 Library.
[26]N. Guler, P. Volegov, C. R. Danly, G. P. Grim, F. E. Merrill, and C. H. Wilde, "Simultaneous usage of pinhole and penumbral apertures for imaging small scale neutron sources from inertial confinement fusion experiments," Rev. Sci. Instrum. **83**, 10D316-1–3 (2012).
[27]T. Ma, N. Izumi, R. Tommasini, D. K. Bradley, P. Bell, C. J. Cerjan, S. Dixit, T. Döppner, O. Jones, J. L. Kline, G. Kyrala, O. L. Landen, S. LePape, A. J. Mackinnon, H.-S. Park, P. K. Patel, R. R. Prasad, J. Ralph, S. P. Regan, V. A. Smalyuk, P. T. Springer, L. Suter, R. P. J. Town, S. V. Weber, and S. H. Glenzer, "Imaging of high-energy x-ray emission from cryogenic thermonuclear fuel implosions on the NIF," Rev. Sci. Instrum. **83**, 10E115 (2012).
[28]D. C. Wilson, T. N. Arhculeta, R. J. Aragonez, D. P. Atkinson, M. A. Barrios, S. H. Batha, D. E. Bower, D. K. Bradley, R. A. Buckles, D. D. Clark, D. S. Clark, D. J. Clark, J. R. Cradick, C. R. Danly, J. M. Dzenitis, O. B. Drury, R. D. Day, V. E. Fatherley, B. Felker, J. P. Finch, D. N. Fittinghoff, M. Frank, F. P. Garcia, G. P. Grim, R. A. Gallegos, S. M. Glenn, N. Guler, A. H. Hsu, N. Izumi, S. A. Jaramillo, O. S. Jones, M. I. Kauffman, G. A. Kyrala, S. L. Pape, S. N. Liddick, E. N. Loomis, S. S. Lutz, T. Ma, A. J. Mackinnon, R. M. Malone, M. M. Marinak, P. McKenty, D. Mares, D. D. Martinson, N. S. Meezan, F. E. Merrill, M. J. Moran, G. L. Morgan, C. Munson, T. J. Murphy, J. A. Oertel, M. V. Patel, P. J. Polk, G. P. Roberson, D. W. Schmidt, S. M. Sepke, B. K. Spears, R. Tommasini, A. Traille, I. L. Tregillis, A. C. Valdez, P. L. Volegov, T.-S. F. Wang, P. Weiss, C. H. Wilde, and M. D. Wilke, "Comparison of neutron and x-ray emission from NIF implosions," Eur. J. Phys. (submitted).
[29]O. S. Jones, C. J. Cerjan, M. M. Marinak, J. L. Milovich, H. F. Robey, P. T. Springer, L. R. Benedetti, D. L. Bleuel, E. J. Bond, D. K. Bradley, D. A. Callahan, J. A. Caggiano, P. M. Celliers, D. S. Clark, S. M. Dixit, T. Doppner, R. J. Dylla-Spears, E. G. Dzentitis, D. R. Farley, S. M. Glenn, S. H. Glenzer, S. W. Haan, B. J. Haid, C. A. Haynam, D. G. Hicks, B. J. Kozioziemski, K. N. LaFortune, O. L. Landen, E. R. Mapoles, A. J. MacKinnon, J. M. McNaney, N. B. Meezan, P. A. Michel, J. D. Moody, M. J. Moran, D. H. Munro, M. V. Patel, T. G. Parham, J. D. Sater, S. M. Sepke, B. K. Spears, R. P. J. Town, S. V. Weber, K. Widmann, C. C. Widmayer, E. A. Williams, L. J. Atherton, M. J. Edwards, J. D. Lindl, B. J. MacGowan, L. J. Suter, R. E. Olson, H. W. Herrmann, J. L. Kline, G. A. Kyrala, D. C. Wilson, J. Frenje, T. R. Boehly, V. Glebov, J. P. Knauer, A. Nikroo, H. Wilkens, and J. D. Kilkenny, "A high-resolution integrated model of the national ignition campaign cryogenic layered experiments," Phys. Plasmas **19**, 056315 (2012).
[30]H. F. Robey, T. R. Boehly, P. M. Celliers, J. H. Eggert, D. Hicks, R. F. Smith, R. Collins, M. W. Bowers, K. G. Krauter, P. S. Datte, D. H. Munro, J. L. Milovich, O. S. Jones, P. A. Michel, C. A. Thomas, R. E. Olson, S. Pollaine, R. P. J. Town, S. Haan, D. Callahan, D. Clark, J. Edwards, J. L. Kline, S. Dixit, M. B. Schneider, E. L. Dewald, K. Widmann, J. D. Moody, T. Döppner, H. B. Radousky, A. Throop, D. Kalantar, P. DiNicola, A. Nikroo, J. J. Kroll, A. V. Hamza, J. B. Horner, S. D. Bhandarkar, E. Dzenitis, E. Alger, E. Giraldez, C. Castro, K. Moreno, C. Haynam, K. N. LaFortune, C. Widmayer, M. Shaw, K. Jancaitis, T. Parham, D. M. Holunga, C. F. Walters, B. Haid, E. R. Mapoles, J. Sater, C. R. Gibson, T. Malsbury, J. Fair, D. Trummer, K. R. Coffee, B. Burr, L. V. Berzins, C. Choate, S. J. Brereton, S. Azevedo, H. Chandrasekaran, D. C. Eder, N. D. Masters, A. C. Fisher, P. A. Sterne, B. K. Young, O. L. Landen, B. M. V. Wonterghem, B. J. MacGowan, J. Atherton, J. D. Lindl, D. D. Meyerhofer, and E. Moses, "Shock timing experiments on the national ignition facility: Initial results and comparison with simulation," Phys. Plasmas **19**, 042706 (2012).
[31]D. G. Hicks, B. K. Spears, D. G. Braun, R. E. Olson, C. M. Sorce, P. M. Celliers, G. W. Collins, and O. L. Landen, "Convergent ablator performance measurements," Phys. Plasmas **17**, 102703 (2010).
[32]D. A. Callahan, N. B. Meezan, S. H. Glenzer, A. J. MacKinnon, L. R. Benedetti, D. K. Bradley, J. R. Celeste, P. M. Celliers, S. N. Dixit, T. Döppner, E. G. Dzentitis, S. Glenn, S. W. Haan, C. A. Haynam, D. G. Hicks, D. E. Hinkel, O. S. Jones, O. L. Landen, R. A. London, A. G. MacPhee, P. A. Michel, J. D. Moody, J. E. Ralph, H. F. Robey, M. D. Rosen, M. B. Schneider, D. J. Strozzi, L. J. Suter, R. P. J. Town, K. Widmann, E. A. Williams, M. J. Edwards, B. J. MacGowan, J. D. Lindl, L. J. Atherton, G. A. Kyrala, J. L. Kline, R. E. Olson, D. Edgell, S. P. Regan, A. Nikroo, H. Wilkins, J. D. Kilkenny, and A. S. Moore, "The velocity campaign for ignition on NIF," Phys. Plasmas **19**, 056305 (2012).
[33]D. Clark, D. E. Hinkel, D. C. Eder, O. S. Jones, S. W. Haan, B. A. Hammel, M. M. Marinak, J. L. Milovich, H. F. Robey, L. J. Suter, and R. P. J. Town, "Detailed implosion modeling of deuterium-tritium layered experiments on the National Ignition Facility," Phys. Plasmas **20**, 056318 (2013).
[34]V. Glebov, D. Meyerhofer, T. Sangster, C. Stoeckl, S. Roberts, C. Barrera, J. Celeste, C. Cerjan, L. Dauffy, D. Eder, R. Griffith, S. Haan, B. Hammel, S. Hatchett, N. Izumi, J. Kimbrough, J. Koch, O. Landen, R. Lerche, B. MacGowan, M. Moran, E. Ng, T. Phillips, P. Song, R. Tommasini, B. Young, S. Caldwell, G. Grim, S. Evans, J. Mack, T. Sedillo, M. Wilke, D. Wilson, C. Young, D. Casey, J. Frenje, C. Li, R. Petrasso, F. Seguin, J. Bourgade, L. Disdier, M. Houry, I. Lantuejoul, O. Landoas, G. Chandler, G. Cooper, R. Leeper, R. Olson, C. Ruiz, M. Sweeney, S. Padalino, C. Horsfield, and B. Davis, "Development of nuclear diagnostics for the national ignition facility (invited)," Rev. Sci. Instrum. **77**, 10E715-1–7 (2006).
[35]D. L. Bleuel, C. B. Yeamans, L. A. Bernstein, R. M. Bionta, J. A. Caggiano, D. T. Casey, G. W. Cooper, O. B. Drury, J. A. Frenje, C. A. Hagmann, R. Hatarik, J. P. Knauer, M. G. Johnson, K. M. Knittel, R. J. Leeper, J. M. McNaney, M. Moran, C. L. Ruiz, and D. H. G. Schneider, "Neutron activation diagnostics at the national ignition facility (invited)," Rev. Sci. Instrum. **83**, 10D313 (2012).